



**AFRL-RZ-WP-TP-2010-2088**

**DYNAMIC FIELD AND CURRENT DISTRIBUTIONS IN  
MULTIFILAMENTARY  $\text{YBa}_2\text{Cu}_3\text{O}_{7-\delta}$  THIN FILMS WITH  
MAGNETIC COUPLING (POSTPRINT)**

**Andrea Lucarelli, Ran Yang, and Gunter Lüpke**

**The College of William and Mary**

**Francesco Grilli**

**Ecole Polytechnique de Montréal**

**Timothy Haugan and Paul Barnes**

**Mechanical Energy Conversion Branch**

**Energy/Power/Thermal Division**

**MARCH 2010**

**Approved for public release; distribution unlimited.**

*See additional restrictions described on inside pages*

**STINFO COPY**

**© 2009 American Institute of Physics**

**AIR FORCE RESEARCH LABORATORY  
PROPULSION DIRECTORATE  
WRIGHT-PATTERSON AIR FORCE BASE, OH 45433-7251  
AIR FORCE MATERIEL COMMAND  
UNITED STATES AIR FORCE**

REPORT DOCUMENTATION PAGE				Form Approved OMB No. 0704-0188	
<p>The public reporting burden for this collection of information is estimated to average 1 hour per response, including the time for reviewing instructions, searching existing data sources, gathering and maintaining the data needed, and completing and reviewing the collection of information. Send comments regarding this burden estimate or any other aspect of this collection of information, including suggestions for reducing this burden, to Department of Defense, Washington Headquarters Services, Directorate for Information Operations and Reports (0704-0188), 1215 Jefferson Davis Highway, Suite 1204, Arlington, VA 22202-4302. Respondents should be aware that notwithstanding any other provision of law, no person shall be subject to any penalty for failing to comply with a collection of information if it does not display a currently valid OMB control number. <b>PLEASE DO NOT RETURN YOUR FORM TO THE ABOVE ADDRESS.</b></p>					
1. REPORT DATE (DD-MM-YY) March 2010		2. REPORT TYPE Journal Article Postprint		3. DATES COVERED (From - To) 16 September 2007 – 16 September 2009	
4. TITLE AND SUBTITLE DYNAMIC FIELD AND CURRENT DISTRIBUTIONS IN MULTIFILAMENTARY YBa <sub>2</sub> Cu <sub>3</sub> O <sub>7-δ</sub> THIN FILMS WITH MAGNETIC COUPLING (POSTPRINT)				5a. CONTRACT NUMBER In-house	
				5b. GRANT NUMBER	
				5c. PROGRAM ELEMENT NUMBER 62203F	
6. AUTHOR(S) Andrea Lucarelli, Ran Yang, and Gunter Lüpke (The College of William and Mary) Francesco Grilli (Ecole Polytechnique de Montréal) Timothy Haugan and Paul Barnes (AFRL/RZPG)				5d. PROJECT NUMBER 3145	
				5e. TASK NUMBER 32	
				5f. WORK UNIT NUMBER 314532ZE	
7. PERFORMING ORGANIZATION NAME(S) AND ADDRESS(ES) The College of William and Mary Department of Applied Science Williamsburg, VA 23187-8795 ----- Ecole Polytechnique de Montréal P.O. Box 6079 Station Centre-Ville Montréal, Quebec H3C 3A7 Canada				8. PERFORMING ORGANIZATION REPORT NUMBER AFRL-RZ-WP-TP-2010-2088	
9. SPONSORING/MONITORING AGENCY NAME(S) AND ADDRESS(ES) Air Force Research Laboratory Propulsion Directorate Wright-Patterson Air Force Base, OH 45433-7251 Air Force Materiel Command United States Air Force				10. SPONSORING/MONITORING AGENCY ACRONYM(S) AFRL/RZPG	
				11. SPONSORING/MONITORING AGENCY REPORT NUMBER(S) AFRL-RZ-WP-TP-2010-2088	
12. DISTRIBUTION/AVAILABILITY STATEMENT Approved for public release; distribution unlimited.					
13. SUPPLEMENTARY NOTES Journal article published in the <i>Journal of Applied Physics</i> , Vol. 106 (2009). PA Case Number: 88ABW-2009-2165; Clearance Date: 18 November 2008. © 2009 American Institute of Physics. The U.S. Government is joint author of the work and has the right to use, modify, reproduce, release, perform, display, or disclose the work.					
14. ABSTRACT We report on the effects of different multifilamentary geometries on the dynamic current and field distributions in YBa <sub>2</sub> Cu <sub>3</sub> O <sub>7-δ</sub> thin films. Finite-element model simulations are presented that allow a direct comparison of the calculated magnetic flux and current profiles with experimental data obtained by time-resolved magneto-optical imaging. We find that increasing the distance between filaments reduces the magnetic coupling and decreases the ac losses. Screening and transport currents also redistribute more evenly between all filaments. The measured transport current density profiles are in good agreement with the modified critical state model.					
15. SUBJECT TERMS superconductivity, critical current density, magnetic field, YBa <sub>2</sub> Cu <sub>3</sub> O <sub>7-z</sub> or YBCO, time-resolved magneto-optical imaging, multifilament wires, ac losses, dynamic current distributions, finite-element model simulations, transport currents, modified critical state model					
16. SECURITY CLASSIFICATION OF:			17. LIMITATION OF ABSTRACT: SAR	18. NUMBER OF PAGES 14	19a. NAME OF RESPONSIBLE PERSON (Monitor) Timothy J. Haugan 19b. TELEPHONE NUMBER (Include Area Code) N/A
a. REPORT Unclassified	b. ABSTRACT Unclassified	c. THIS PAGE Unclassified			

# Dynamic field and current distributions in multifilamentary $\text{YBa}_2\text{Cu}_3\text{O}_{7-\delta}$ thin films with magnetic coupling

Andrea Lucarelli,<sup>1</sup> Ran Yang,<sup>1</sup> Francesco Grilli,<sup>2</sup> Timothy Haugan,<sup>3</sup> Paul Barnes,<sup>3</sup> and Gunter Lüpke<sup>1,a)</sup>

<sup>1</sup>Department of Applied Science, The College of William and Mary, Williamsburg, Virginia 23187-8795, USA

<sup>2</sup>Ecole Polytechnique de Montréal, P.O. Box 6079, Station Centre-Ville, Montréal, Quebec H3C 3A7, Canada

<sup>3</sup>Air Force Research Laboratory, Wright-Patterson AFB, Ohio 45433-7919, USA

(Received 3 April 2009; accepted 31 July 2009; published online 16 September 2009)

We report on the effects of different multifilamentary geometries on the dynamic current and field distributions in  $\text{YBa}_2\text{Cu}_3\text{O}_{7-\delta}$  thin films. Finite-element model simulations are presented that allow a direct comparison of the calculated magnetic flux and current profiles with experimental data obtained by time-resolved magneto-optical imaging. We find that increasing the distance between filaments reduces the magnetic coupling and decreases the ac losses. Screening and transport currents also redistribute more evenly between all filaments. The measured transport current density profiles are in good agreement with the modified critical state model. © 2009 American Institute of Physics. [doi:10.1063/1.3212976]

## I. INTRODUCTION

The separation of high-temperature superconducting (HTS) tapes into filaments is a viable approach to reduce ac and hysteretic losses in high-power applications, where alternating currents and magnetic fields are present simultaneously.<sup>1</sup> Methods such as mechanical<sup>2</sup> or laser scribing,<sup>3</sup> photolithography,<sup>4</sup> or direct printing on buffered substrates using inkjet deposition<sup>5</sup> have been used to create the filamentary structure in second-generation HTS coated conductors. However, ac losses of finely striated tapes can still be larger than desired as predicted by analytical expressions.<sup>6</sup> Even so, the magnetic field concentration in the nonsuperconducting trenches influences the flux distribution inside the superconducting filaments, and this magnetic coupling ultimately creates losses that depend on the distance between filaments. This is a complex nonlinear problem that necessitates an in-depth understanding of the flux and current dynamics in multifilamentary HTS structures as both depend strongly on temperature and history of the applied field and transport current.

In this paper we report on the effects of different multifilamentary geometries on the dynamic current and field distributions in  $\text{YBa}_2\text{Cu}_3\text{O}_{7-\delta}$  (YBCO) thin films. We present finite-element model (FEM) simulations that allow a direct comparison of the calculated magnetic flux and current profiles with experimental data obtained by time-resolved magneto-optical imaging (TRMOI). The comparison provides both a test of the model itself as well as new information on the complex behavior of YBCO thin films observed previously.<sup>7</sup> We find for filamentary samples where the ends of the filaments on each side are connected via the superconducting film, see Fig. 1, that increasing the spacing reduces the magnetic coupling between filaments, which respond

more independently to an applied field and ac. Screening and transport currents also redistribute more evenly between all filaments. The reduced magnetic coupling affects field and current dynamics and decreases ac losses.

## II. MODELING

In the FEM simulation we neglect thermal aspects and focus on the electromagnetic behavior. The superconducting film is considered to be at a constant operating temperature below the critical temperature, and no quenching occurs. In addition, since the samples are long and straight, we utilize a two-dimensional model considering only the superconducting cross section. The electromagnetic behavior is described by Faraday's law

$$\nabla \times \vec{E} = -\frac{\partial \vec{B}}{\partial t}. \quad (1)$$

The superconducting property is incorporated by means of a nonlinear relation between electric field and current density

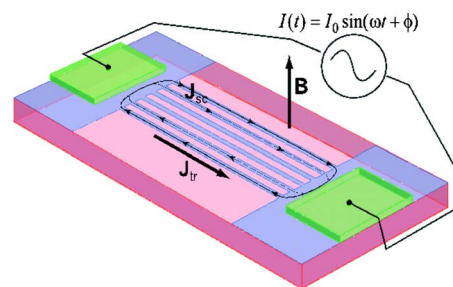


FIG. 1. (Color online) Example of a filamentary YBCO thin film (blue area) grown on an insulating substrate (pink) with metal contact pads (green). The dc field  $B$  is applied perpendicularly to the film. The screening current  $J_{sc}$  flows circularly in the sample, while the ac transport current  $J_{tr}$  flows along the filaments.

<sup>a)</sup>Electronic mail: luepke@wm.edu.

$$\rho(J) = \frac{E_c}{J_c} \left| \frac{J}{J_c} \right|^{n-1}. \quad (2)$$

This relation describes quite well the experimental current-voltage characteristics of superconducting samples. The power index  $n$  represents the steepness of the transition from superconducting to normal state and is indicative of the physical phenomena of flux flow and flux creep.<sup>8</sup> In high-temperature and type-II superconductors, magnetic flux lines enter as quantized vortices at very small values of the magnetic field  $B_{c1}$ . For this reason in the simulation we express the  $B$ - $H$  relation by using  $B = \mu_0 H$ .<sup>9</sup>

The model is implemented in COMSOL's general partial differential equation (PDE) module and uses two magnetic field components as state variables. First-order edge elements are used to satisfy the zero-divergence equation for the magnetic field. Details about the model implementation are given in Ref. 10. The external magnetic field is incorporated by using Dirichlet boundary conditions in the air domain. The transport current is included by using integral constraints in COMSOL's point settings. The integral constraints introduce coupling between filaments corresponding to the superconductive region connecting the filaments in the sample as depicted in Fig. 1.

In the FEM simulations, we consider a system consisting of the air domain and six superconducting filaments connected at the ends. The dimensions chosen for the system correspond to YBCO thin films grown by pulsed laser deposition on a  $\text{LaAlO}_3$  or  $\text{SrTiO}_3$  substrate and patterned by photolithography to obtain a multifilamentary structure (Fig. 1). Since the substrate has very poor conductivity and is nonmagnetic, it has been neglected in the simulated geometry. These films have been previously studied by TRMOI under the same experimental conditions used in the simulations.<sup>11</sup>

The model is not restricted to any number of filaments, dimensions, or aspect ratios. However, a high aspect ratio of the thin film geometry introduces a large number of nodes that can severely affect the computation time especially for systems with a large number of filaments. The simulation of two cycles takes about 3–4 h on a workstation equipped with a 2.4 GHz processor and 3 Gbytes of random access memory. In order to avoid transient effects, three complete cycles of the current in 50 steps are simulated. An example of the simulated geometry and corresponding mesh is depicted in Fig. 2(a). The circular outer boundary for the air domain is used to impose Dirichlet boundary conditions. The density of nodes in the mesh increases near the filaments as shown in the detailed view of Fig. 2(b).

In order to allow direct comparison between FEM simulations and TRMOI measurements of the field dynamics, we calculate the magnetic profiles at a height of 1  $\mu\text{m}$  over the sample surface [see Fig. 2(b)]. This approach has two implications. First, it reduces slightly the intensity of the simulated field profiles, similarly to what occurs in the actual measurements, and second, it roughens the profiles adding noise due to the coarsening of the mesh. The latter effect could be avoided by refining the mesh in that region but at the cost of an increased calculation time.

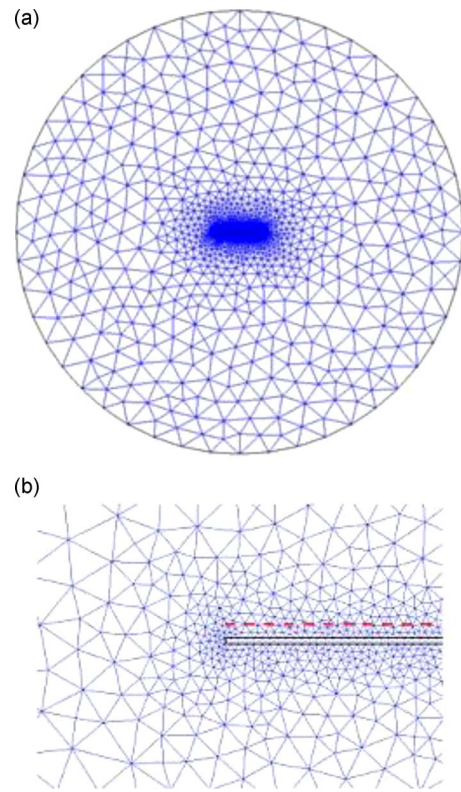


FIG. 2. (Color online) (a) Complete mesh and (b) a detailed view near the edge of a superconducting filament. The red dashed line indicates the region of the simulated field profiles.

### III. EXPERIMENTAL

In our TRMOI experiments, the sample size is normally  $5 \times 12 \text{ mm}^2$  with six filaments. The striation is made by photolithography and wet etching. The average width, spacing, and length of the filaments are 130  $\mu\text{m}$ , 200  $\mu\text{m}$ , and 4 mm, respectively. Figure 1 displays a schematic three-dimensional drawing of the samples where the blue areas indicate the superconducting YBCO film, which is about 300 nm thick grown on a  $\text{SrTiO}_3$  substrate. The samples exhibit a critical transition temperature ( $T_c$ ) of 91 K with a sharp transition within  $2^\circ$  (at 2.2 Oe loss data) as determined by ac susceptibility measurements. The samples are carefully inspected for defects, which may couple two neighboring filaments (other than the end caps) or discontinue the current flow in a filament.

In the TRMOI experiment, the sample is zero-field cooled to 15 K and then a dc magnetic field of  $B_d = 5 \text{ mT}$  is applied perpendicular to the YBCO film together with a sinusoidal ac transport current  $I_0 = 8 \text{ A}$  at a frequency  $f = 1000 \text{ Hz}$ . The TRMOI experiment is described in detail in Ref. 11. Figure 3 displays images taken from a six-filament YBCO sample at different phase points of the ac transport current. Bright areas in the image correspond to regions of high magnetic flux density near the edges of the filaments. The dark areas in the center of the image indicate flux-free regions. The uniformly gray region (red in the online version) represents the intermediate magnetic field outside the sample. Positive and symmetric flux penetrations occur on both sides of the sample due to the applied dc field (Fig. 3,



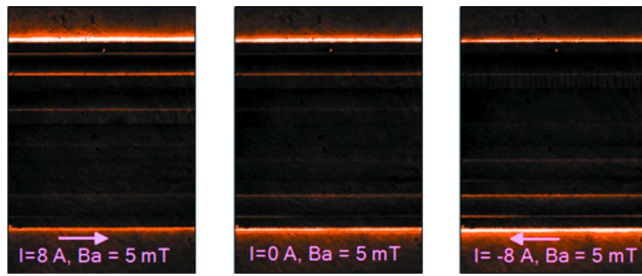


FIG. 3. (Color online) TRMOI images from a six-filament YBCO thin film for different phase points of the applied ac with  $I_0=8$  A. A dc magnetic field of 5 mT is applied perpendicular to the film. The arrow indicates the current direction.

middle image). Additional flux penetrates at the top edge of the filaments when a transport current flows in the positive direction (Fig. 3, left image), while the same effect occurs at the bottom edge when the current flows in the negative direction (Fig. 3, right image). This phenomenon is most pronounced for the outer filaments.

#### IV. RESULTS

Figure 4 (top) shows the magnetic flux distribution calibrated from light intensity profiles of the TRMOI measure-

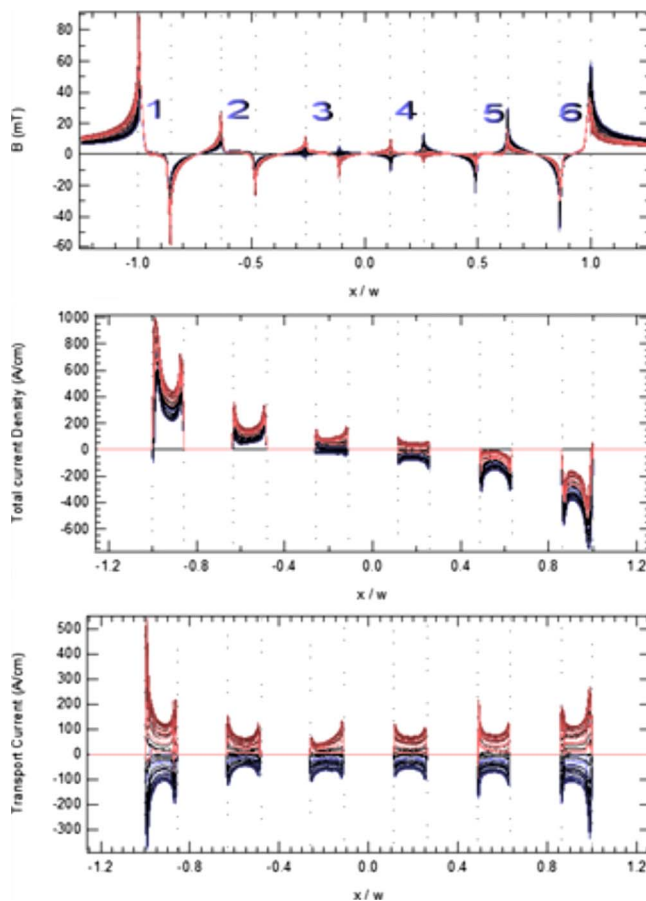


FIG. 4. (Color online) The magnetic field distribution (top), the total current distribution (middle), and the transport current distribution (bottom) of the six-filament YBCO sample with applied ac ( $I_0=8$  A) and perpendicular dc magnetic field ( $B_a=5$  mT). The positive-to-negative ac cycles are colored in red-black-blue shades. The vertical dotted lines indicate the edges of each filament.

ments. The magnetic flux changes its sign and amplitude with the phase evolution of the ac. The positive flux has a higher absolute value than the negative flux because the external field is static and always contributes a positive flux. The total current distributions are shown in Fig. 4 (middle) obtained by numerical inversion of Biot–Savart law from the magnetic field distributions. The total current flowing in the first three filaments 1–3 is mostly positive while it is predominantly negative in filaments 4–6. For all 51 phase-dependent profiles, the current distribution outside of the six superconducting filaments is set to zero, which has only a small effect on the total current density as shown further below. The transport current distributions shown in Fig. 4 (bottom) are calculated by subtracting the shielding current determined from the current distribution at zero phase point. As expected, in the positive (negative) half-period, only positive (negative) current (red shades) flows through all six filaments.

Figure 5 shows the total transport current flowing in all six filaments at each phase point (red dots). The current oscillates between  $-7.72$  and  $8.33$  A (black dashed line), which is in good agreement with the experimental value  $I_0=8$  A. This result shows that the current distributions obtained from the TRMOI measurements are quite accurate. For the multifilamentary film, when the filaments are not coupled, the current will evenly distribute between all filaments. On the other hand, when the filaments are coupled, the current flows across the transverse resistance between filaments<sup>12</sup> for resistive interfilamentary connections or, in this case, via superconducting connections at the ends. Although these two different types of connection (superconducting and nonsuperconducting) will have a different effect on the current distribution, they both will result in nonuniform current distribution across the filaments. Figure 6 displays the transport current distribution (solid lines) at two extreme phase points,  $\phi=90^\circ$  and  $270^\circ$ , which clearly reveals that the six filaments are coupled in our experiment.

#### V. COMPARISON OF MODEL TO EXPERIMENT

To further analyze the current distribution, we use the modified critical state model (CSM) for the superconducting thin film geometry with an applied ac and a static magnetic field applied perpendicular to the sample face.<sup>11</sup> The blue and red dashed lines are fits of the modified CSM for a single-bridged sample, which indicates the overall current density distribution across all filaments. The green dotted curves represent fits of individual filaments, which agree fairly well with the measured data in shape and amplitude. Compared to the transport current values calculated from the measured data, the average error is approximately 15%.

We also compare the TRMOI data with FEM simulation data. Figure 7 shows the magnetic field distribution (top) and the total current distribution (bottom) obtained from FEM calculations. The parameters for the FEM simulation are the same as in the measurement  $B_a=5$  mT and  $I_0=8$  A at 1000 Hz. However, the critical current density,  $J_c=4.1$

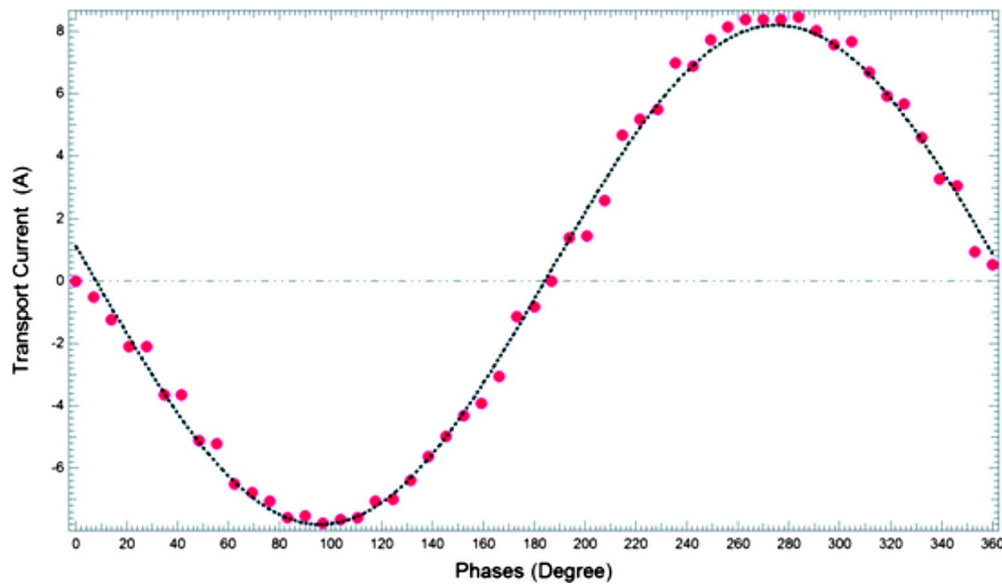


FIG. 5. (Color online) The integrated transport current (red dots) in the six-filament YBCO sample and best fit to a sinusoidal curve (dashed black line).

$\times 10^7 \text{ A cm}^{-2}$ , is more than twice the value of the single-bridged YBCO thin film. The increase in  $J_c$  is unexpected and requires further investigation.

Figure 8 shows a comparison between FEM simulations (dashed lines) and the TRMOI data (solid lines) for the magnetic field distributions (top) and the total current density profiles (bottom) at three phase points:  $\phi=90^\circ$  (blue),  $\phi=270^\circ$  (red), and  $\phi=180^\circ$  (green). The profiles match quite well for the field distributions. The peaks are higher in the FEM simulation than in the TRMOI data. Moreover, the measured field penetrates further inside of the superconducting filaments. This behavior is also apparent in the current density profiles. For example, in the center of the first filament, the saddle shape total current density profiles have lower values for the FEM simulations than the measured data. This implies that the  $J_c$  used in the FEM simulation is a

little higher than in the experimental data. The FEM simulation also has higher absolute peak amplitudes than the TRMOI data, which also means that the FEM simulation has slightly higher  $J_c$ . Nevertheless, the data from the multifilamentary sample yield a critical current density at least twice as large as the  $J_c$  of single-bridged YBCO thin films, which is a significant advantage of the multifilamentary film.

## VI. EFFECT OF FILAMENT SPACING

Next, we investigate the effect of magnetic coupling between superconducting filaments by studying the dynamic current and field distributions as a function of distance between filaments. The width of the filaments is fixed at  $120 \text{ } \mu\text{m}$  while the spacing is varied. We simulated three different geometries with width/distance ratios 8/1, 4/1, and 2/1,

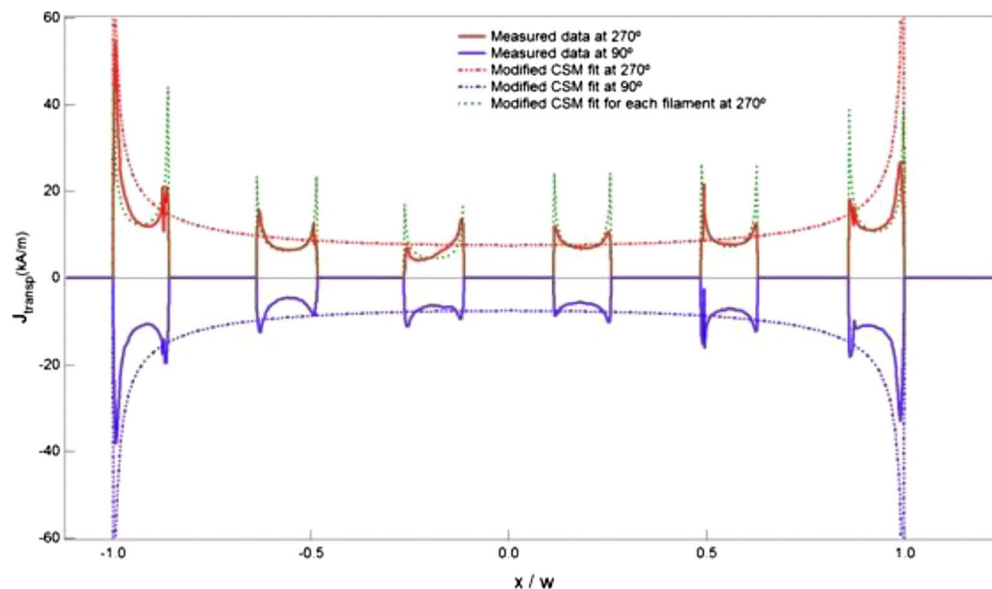


FIG. 6. (Color online) Comparison between measured transport current density profiles (solid lines) and fits of the modified CSM model (dotted lines) for two phase points:  $90^\circ$  and  $270^\circ$ .

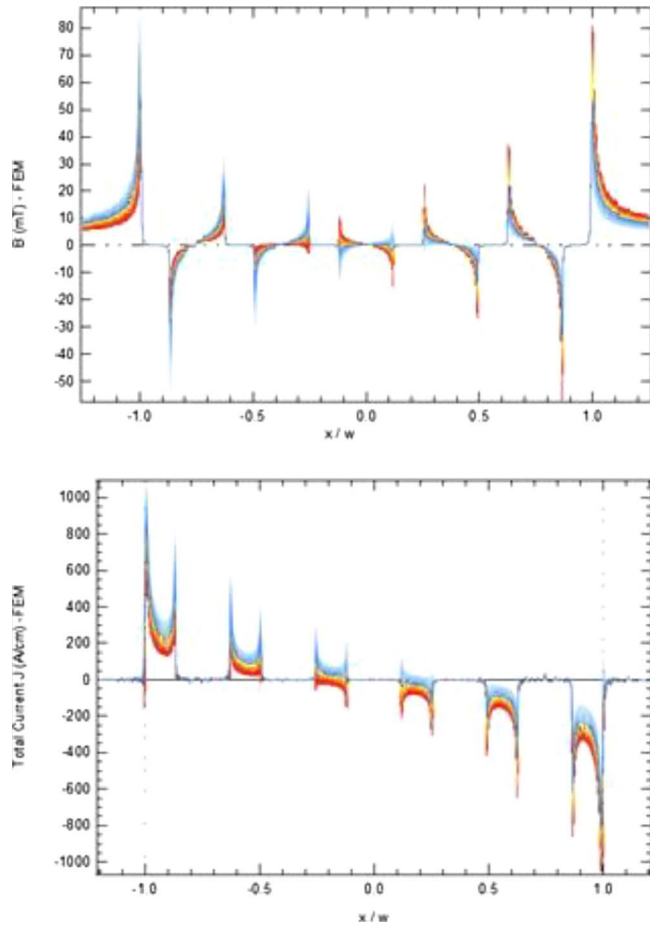


FIG. 7. (Color online) FEM simulation of the magnetic field distribution (top) and the total current distribution (bottom) for the six-filament YBCO sample with applied ac ( $I_0=8$  A) and perpendicular dc magnetic field ( $B_d=5$  mT). The positive-to-negative ac cycles are colored in red-yellow-blue shades. The vertical dotted lines indicate the outer edges of the six filaments.

comparable to multifilamentary coated conductors reported in literature.<sup>2-6</sup> The applied field intensity is 5 mT and the ac  $I(t)=I_0 \sin(2\pi ft)$  has an amplitude  $I_0=8$  A and a frequency  $f=1000$  Hz. For the superconducting material, we choose  $J_c=3 \times 10^{11}$  A/m<sup>2</sup>,  $E_c=10^{-4}$  V/m, and  $n=25$ , which are typical values for YBCO thin films at about 30 K.

### A. Simulation

In Fig. 9 we present field profiles at different phase points for three different geometries used in the simulations. We also plot magnetic flux distributions as time-dependent field maps in Figs. 9(d)–9(f) to present more clearly the time variations of the field. The magnetic flux partially penetrates into the filaments from the edges forming flux fronts. These regions, as well as the flux-free regions (Meissner state), remain constant during the cycle in all the filaments for the three different geometries shown in Figs. 9(a)–9(c). The flux profiles at the edges of the filaments alter during the cycle due to the self-field of the applied ac. The magnetic flux distribution changes also for the three different geometries. Increasing the filament distance allows more flux to penetrate into the space between the filaments. Here, the peak intensity of the field profiles grows linearly with distance [Figs. 9(b) and 9(c)]. The flux profiles reach their maximum

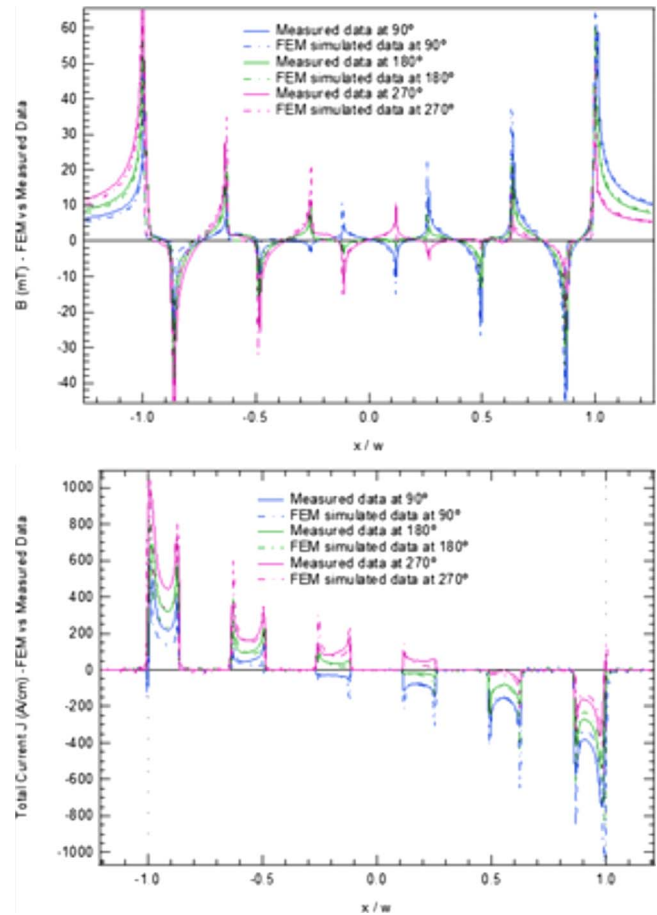


FIG. 8. (Color online) Comparison between FEM simulations (dashed lines) and measured magnetic field distribution (top) and total current distribution (bottom) for three phase points:  $\phi=90^\circ$  (blue),  $\phi=180^\circ$  (green), and  $\phi=270^\circ$  (red).

value of 65 mT at the edges of the two outer filaments. The change in geometry does not affect the maximum value of the peaks in the flux profiles, but it alters the dips that form at the external edges of the outer filaments, as indicated by black arrows in Figs. 9(a)–9(c). This reveals how the sample screens the external magnetic flux for the different geometries. As the filament spacing increases the coupling between filaments is reduced and the screening behavior becomes more similar to independent filaments.

The current dynamics provides additional useful information regarding the coupling between filaments. Figure 10 shows the current density profiles at different phase points and the corresponding time-dependent field maps. The maps show at first glance how the current in each filament changes sign during each cycle, passing from positive (red) through zero (white) to negative (blue). Interestingly, a “return current” of opposite sign [black arrows in Figs. 10(a)–10(c)] flows in a narrow region at the edges of the left outer filament in the first half cycle ( $-180^\circ < \phi < 0^\circ$ ) and on the right outer filament in the second half cycle ( $0^\circ < \phi < 180^\circ$ ). This current causes the steep variation from positive to negative flux observed in the same region of the field profiles (Fig. 9). A similar behavior has been observed in TRMOI measurements of single-bridged YBCO thin films.<sup>13</sup> The return current is reduced by increasing the spacing between the fila-



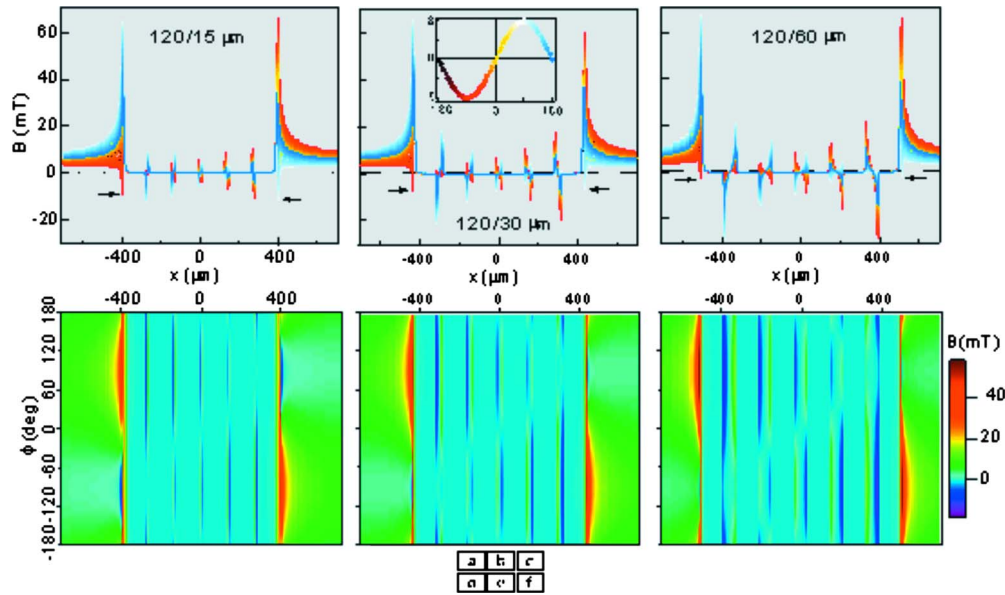


FIG. 9. (Color online) Magnetic field profiles at different phase points and corresponding time-dependent intensity maps for three multifilamentary geometries with filament/groove ratios corresponding to 8/1 [(a) and (d)], 4/1 [(b) and (e)], and 2/1 [(c) and (f)].

ments from 15 to 60  $\mu\text{m}$ . The increased distance reduces the coupling between the filaments and redistributes the screening currents between the filaments. The growth of the peak intensity at the edges of all the filaments reveals the reduced coupling between filaments. For the three different geometries the current density in the two outer filaments shows the most intense value corresponding to the critical current density  $J_c = 3 \times 10^{11}$  A/m<sup>2</sup>, as predicted by the CSM. This result yields further proof of the accuracy of our method.

## B. Comparison to experiment

The current density profiles shown in Fig. 10 are obtained from the field profiles by inversion of Biot–Savart law. This method has some limitations but it allows direct comparison of the simulated results with experimental measurements. The current profiles obtained by the inversion method differ only slightly from those calculated directly by the COMSOL model. This procedure does not change the overall

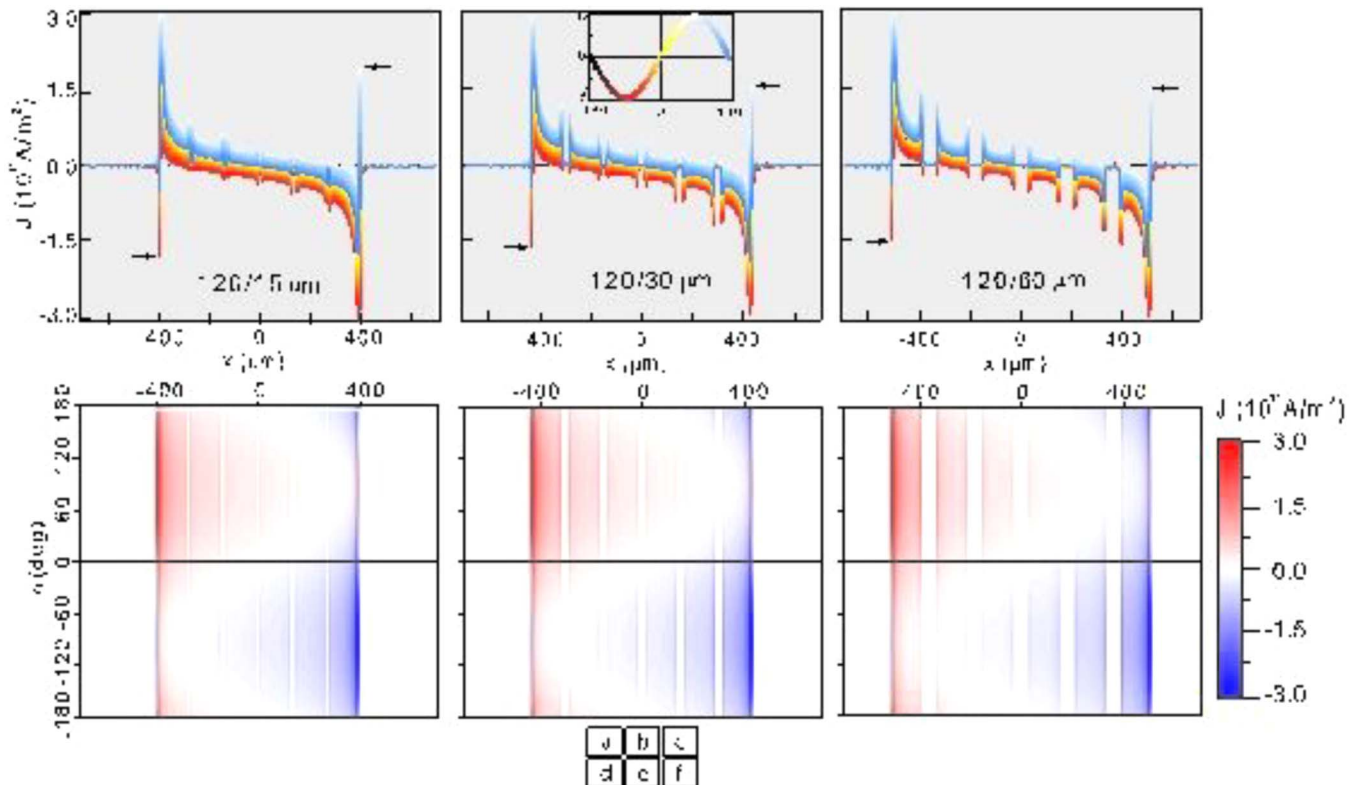


FIG. 10. (Color online) Current density profiles at different phase points and corresponding time-dependent intensity maps for three multifilamentary geometries with filament/groove ratios corresponding to 8/1 [(a) and (d)], 4/1 [(b) and (e)], and 2/1 [(c) and (f)].



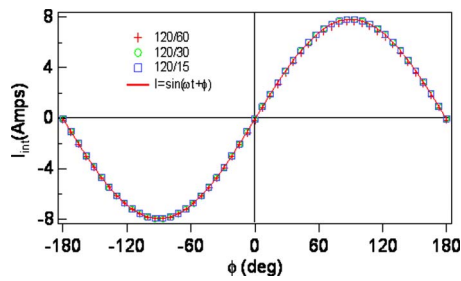


FIG. 11. (Color online) Total current flowing in all filaments calculated at different phase points for three different geometries (symbols) and best fit (solid line).

shape of the current profiles, nor does it affect their time-dependent behavior, but it smoothes and partially reduces the intensity of the peaks.

Figure 11 shows the integrated current densities at different phase points and best fits for the three geometries used in the simulation. The screening component of the current is symmetric,<sup>13</sup> and thus it cancels out in the integration of the current density over all filaments, and we obtain the transport current. Figure 11 shows that the amplitude and phase of the transport current are not affected by the geometry. This quantitative analysis also confirms that the reduction in current intensity introduced by the inversion method is less than 1.3%.

### C. ac loss consideration

Figure 12 shows the transport current per filament for three different geometries. Only the first three filaments are represented for clarity. The behavior of the other three filaments is completely symmetric. The current flows in each filament without any significant shift in phase with respect to the applied current. The current flows mostly in the outer filaments for all geometries. The 120/60 geometry shows higher values of the current in the internal filaments as compared to the other geometries. As the spacing between filaments is increased the transport current distributes more evenly.

We also use the FEM to calculate the electric field. From the current and electric field profiles, the instantaneous power losses can be calculated using the formula

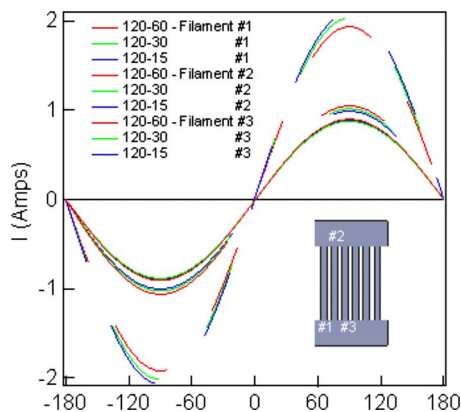


FIG. 12. (Color online) Transport current per filament in the first three filaments (inset) for three different geometries.

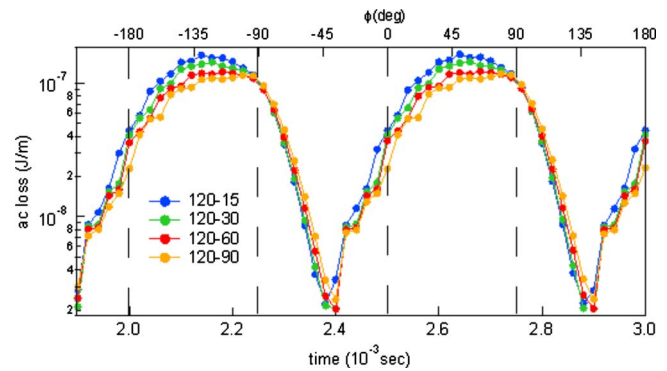


FIG. 13. (Color online) Instantaneous ac losses for four different geometries.

$$P(t) = |J(t) \cdot E(t)|. \quad (3)$$

Figure 13 shows the time-dependent losses for four different geometries with the filament width-distance: 120-15, 120-30, 120-60, and 120-90. The instantaneous losses decrease with increasing filament spacing in the range  $\phi = -36^\circ$  to  $\phi = 90^\circ$ , while in other regions the losses slightly increase. However, the values of the losses integrated over the whole cycle show an effective reduction of about 30% in the 120-90 geometry as compared to 120-15.

## VII. CONCLUSIONS

In summary, we studied dynamic field and current distributions in multifilamentary YBCO thin films by TRMOI and by numerical simulation using COMSOL's PDE module (general form) to solve Maxwell's equations. A comparison of the TRMOI data with FEM simulation shows that the multifilamentary films have at least twice the critical current density  $J_c$  than single-bridged YBCO thin films. Furthermore, an increase in filament spacing alters the field and current dynamics due to reduced magnetic coupling between filaments. Screening and transport currents redistribute more evenly between all filaments, which respond more independently. It also significantly reduces the losses of multifilamentary YBCO thin films.

## ACKNOWLEDGMENTS

This work was supported by the Mathematics of Information Technology and Complex System (MITACS) network. The work at CWM is supported by DOE Grant No. DEFG02-04ER46127.

<sup>1</sup>W. J. Carr and C. E. Oberly, *IEEE Trans. Appl. Supercond.* **9**, 1475 (1999).

<sup>2</sup>S. P. Ashworth and F. Grilli, *Supercond. Sci. Technol.* **19**, 227 (2006).

<sup>3</sup>M. Majoros, B. A. Glowacki, A. M. Campbell, G. A. Levin, P. N. Barnes, and M. Polak, *IEEE Trans. Appl. Supercond.* **15**, 2819 (2005).

<sup>4</sup>D. W. Hazelton, Y. Y. Xie, Y. Qiao, E. Zhang, and V. Selvamanickam, *Adv. Cryog. Eng.* **52**, 859 (2006).

<sup>5</sup>R. C. Duckworth, M. P. Paranthaman, M. S. Bhuiyan, F. A. List, and M. J. Gouge, *IEEE Trans. Appl. Supercond.* **17**, 3159 (2007).

<sup>6</sup>M. D. Sumption, E. W. Collings, and P. N. Barnes, *Supercond. Sci. Technol.* **18**, 122 (2005).

<sup>7</sup>A. Lucarelli, A. Frey, R. Yang, G. Lüpke, F. Grilli, T. J. Haugan, G. A. Levin, and P. Barnes, *Appl. Phys. A: Mater. Sci. Process.* **88**, 601 (2007).

<sup>8</sup>R. P. Huebener, *Magnetic Flux Structures in Superconductors*, 2nd ed.

- (Springer, Berlin, 2001), pp. 245–251.
- <sup>9</sup>J. Paasi and M. Lahtinen, *Physica C* **310**, 57 (1998).
- <sup>10</sup>R. Brambilla, F. Grilli, and L. Martini, *Supercond. Sci. Technol.* **20**, 16 (2007).
- <sup>11</sup>A. Lucarelli, G. Lüpke, T. J. Haugan, G. A. Levin, and P. N. Barnes, *Supercond. Sci. Technol.* **19**, 667 (2006).
- <sup>12</sup>N. Amemiya, S. Kasai, K. Yoda, Z. Jiang, G. A. Levin, P. N. Barnes, and C. E. Oberly, *Supercond. Sci. Technol.* **17**, 1464 (2004).
- <sup>13</sup>A. Lucarelli, A. Frey, R. Yang, G. Lüpke, T. J. Haugan, G. A. Levin, and P. N. Barnes, *Supercond. Sci. Technol.* **21**, 115003 (2008).